INTERNATIONAL JOURNAL FOR NUMERICAL METHODS IN FLUIDS
Int. J. Numer. Meth. Fluids 2006; **52**:473–498
Published online 16 February 2006 in Wiley InterScience (www.interscience.wiley.com). DOI: 10.1002/fld.1167

Simulation of shallow flows over variable topographies using unstructured grids

A. Mohammadian*,† and D. Y. Le Roux‡

Département de Mathématiques et de Statistique, Université Laval, Québec, Que., Canada G1K7P4

SUMMARY

Simulation of shallow flows over variable topographies is a challenging case for most available shock-capturing schemes. This problem arises because the source terms and flux gradients are not balanced in the numerical computations. Treatments for this problem generally work well on structured grids, but they are usually too expensive, and most of them are not directly applicable to unstructured grids. In this paper we propose two efficient methods to treat the source terms without upwinding and to satisfy the compatibility condition on unstructured grids. In the first method, the calculation of the bed slope source term is performed by employing a compatible approximation of water depth at the cell interfaces. In the second one, different components of the bed slope term are considered separately and a compatible discretization of the components is proposed. The present treatments are applicable for most schemes including the Roe's method without changing the performance of the original scheme for smooth topographies. Copyright © 2006 John Wiley & Sons, Ltd.

KEY WORDS: shallow-water; variable topography; unstructured grid; finite volume method

1. INTRODUCTION

The shallow-water (SW) equations govern many practical applications like river and tidal flows in estuary and coastal water regions where variable topographies are usually present. The simulation of these flows is of great interest for hydraulic engineers, particularly on unstructured grids. Unstructured grids are attractive because of their flexibility for representing irregular boundaries and for local mesh refinement. On the other hand, for many fluvial flows, the flow regime changes from subcritical to supercritical and the employed numerical method should be able to solve sub, super and trans-critical flows.

*Correspondence to: A. Mohammadian, Département de Mathématiques et de Statistique, Université Laval, Québec, Que., Canada G1K7P4.
†E-mail: majidm@mat.ulaval.ca
‡E-mail: dleroux@mat.ulaval.ca

Contract/grant sponsor: Natural Science and Engineering Council (NSERC)
Contract/grant sponsor: Fonds Québécois de la Rechersche sur la Nature et les Technologies (FQRNT)

Received 14 September 2004
Revised 19 September 2005
Accepted 26 September 2005

The discretization of the SW equations has received considerable attention in the past two decades and many upwind schemes have successfully solved channel flows [1–4]. However, their use in the presence of irregular topographies is usually problematic, due to *the imbalance between the source terms and the flux gradients* [5]. In fact, most shock-capturing finite volume schemes for the SW equations, are obtained by using approximate Riemann solvers which have been originally designed for hyperbolic systems without considering the source terms (such as bed topography in the case of SW equations). Therefore, in the presence of source terms, those schemes may lead to oscillations. Numerically, this problem is due to an imbalance between discretized source and flux terms.

Some modifications have been brought to the above-mentioned methods in the case of variable topographies and structured grids. For example, the van Leer's Q-scheme was extended by Bermudez and Vazquez-Cendon [5] for the SW equations, and an *upwind discretization of the source terms* for variable topographies has been formulated. The *C* property, which states that the scheme should preserve the stagnant conditions, was also introduced. In the stagnant conditions, water is initially at rest inside of some closed area with variable bottom topography. Hence, without influence from outside, the water should stay at rest. This work has been improved in the case of a general 1D channel with breath variation by Vazquez-Cendon [6]. The Vazquez-Cendon approach was then extended to flux difference splitting schemes by Hubbard and Garcia-Navarro [7]. However, upwinding the source terms is computationally expensive for practical applications because those terms have to be projected on a basis of eigenvectors. LeVeque [8], introduced *a Riemann problem inside a cell* for balancing the source terms and the flux gradients, and the resulting method was found to preserve both *stagnant* and *quasi-steady-state* conditions. However, the LeVeque's scheme is not directly transportable to unstructured grids. On the other side, Kurganov and Levy [9] extended the *central-upwind* (CU) scheme to the SW equations and by using the water surface elevation instead of the depth, they proposed an adaptive algorithm for variable topographies. They also proved that their scheme preserves the steady-state condition with a positive depth, without resorting to any artificial drying and wetting strategies. Unfortunately, their scheme poorly performs in the case of circulating flows, as shown by Mohammadian *et al.* [10]. In a different approach, Alcrudo and Benkhaldon [11] defined the bed level such that a sudden change in the topography occurs at the interface of two cells. They also developed a Riemann solver at the interface with a sudden change in the bed elevation. However, their approach leads to several cases of shock and rarefaction wave patterns and it is numerically too expensive. The ENO and Weighted ENO (WENO) schemes were extended by Vukovic and Sopta [12] to the SW equations including the source terms, but they are restricted to 1D channels. Jin [13] developed the *interface method*, which preserves the steady-state condition up to second-order accuracy on structured grids, but his approach is not directly usable on unstructured grids. A second-order gas kinetic scheme for SW flows over variable topographies was also proposed by Xu [14]. However, the gas kinetic schemes are basically different from characteristics-based schemes and they should be tested for challenging test cases such as recirculating flows. Rogers *et al.* [15], proposed a numerical scheme where the balance is achieved by the incorporation of extra physical information, but, only structured grids are employed. Nujic [16] used the water level variable instead of the depth and he extracted the gravitational terms from the flux functions in the Shu and Osher (SO) scheme [17] to solve for variable topographies. Unfortunately, the SO scheme [17] generates a high level of numerical diffusion in the case of recirculating flows, as shown by Mohammadian *et al.* [10].

Zhou *et al.* [18] introduced the *surface gradient method* where the depth is interpolated at the cell interface considering the bed variations. They showed that by combining their approach with the HLL flux function [19] the C property is satisfied, and the resulting scheme performs well for variable topographies without any extra efforts for balancing the source terms and the flux gradients. However, the C property does not hold on unstructured grids and moreover, the HLL flux induces a high level of numerical viscosity in recirculating flows, as shown in Mohammadian *et al.* [10].

Mohammadian *et al.* [10] showed that the Roe's method produces much less numerical diffusion than the SO, HLL and CU schemes in the case of circulating flows and they developed a numerical scheme using the Roe's method which satisfies the C property. However, although their scheme is mass conservative, it is not fully conservative since the gravity terms are not discretized in a conservative manner.

In this paper we present two efficient numerical methods for flows over variable topographies on unstructured grids. The proposed two methods are shown to satisfy the C property when combined with the Roe's scheme and the surface gradient method [18] for calculating the water depth at the interface. Several numerical tests are presented to show the performance of the two schemes over variable topographies.

The main feature of the methods presented here is that, since they are working directly on the discretization of the source terms, they are not restricted to the Roe's method and they can be used with a large range of existing shock-capturing schemes such as the Roe, the HLL, the HLLC, the CU methods, etc.

This paper is organized as follows. The model equations are introduced in Section 2. The numerical scheme, the treatment of the source term and the proof of the C property are presented in Section 3. In Section 4, some numerical test cases show the performance of the proposed schemes. Some concluding remarks complete the study.

2. GOVERNING EQUATIONS

The 2D SW equations in a conservative form are written as

$$\frac{\partial \mathbf{U}}{\partial t} + \nabla \mathbf{F} = \mathbf{S} + \nabla \mathbf{F}^{\mathrm{d}} \tag{1}$$

with $\mathbf{U}^t = (h, uh, vh)$, $\mathbf{F} = (\mathbf{E}, \mathbf{G})$ and

$$\mathbf{E} = \begin{pmatrix} uh \\ u^2h + 0.5gh^2 \\ uvh \end{pmatrix}, \quad \mathbf{G} = \begin{pmatrix} vh \\ uvh \\ v^2h + 0.5gh^2 \end{pmatrix} \tag{2}$$

where h is the water depth, u and v are the velocity components (Figure 1) and g is the gravitational acceleration.

The superscript d refers to the diffusion and the diffusive flux has the following form:

$$\mathbf{F}^{\mathrm{d}} = (\mathbf{E}^{\mathrm{d}}, \mathbf{G}^{\mathrm{d}}) \tag{3}$$

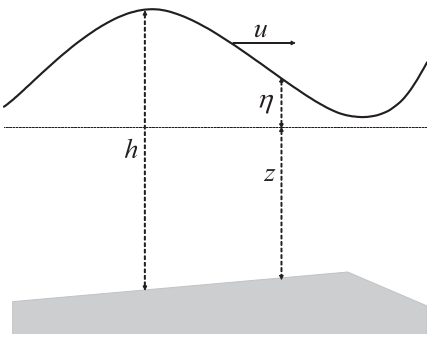

Figure 1. Schematic diagram of an unsteady flow over an irregular bottom and the corresponding notation.

where

$$\mathbf{E}^{\mathrm{d}} = \begin{pmatrix} 0 \\ (v+v_t)h\partial u/\partial x \\ (v+v_t)h\partial v/\partial x \end{pmatrix}, \quad \mathbf{G}^{\mathrm{d}} = \begin{pmatrix} 0 \\ (v+v_t)h\partial u/\partial y \\ (v+v_t)h\partial v/\partial y \end{pmatrix} \tag{4}$$

and v and v_t are water and eddy viscosity coefficients, respectively.

The source term $\mathbf{S}$ is written as

$$\mathbf{S} = \begin{pmatrix} 0 \\ c_{\mathrm{f}} u\sqrt{u^2+v^2} + gh\partial z/\partial x \\ c_{\mathrm{f}} v\sqrt{u^2+v^2} + gh\partial z/\partial y \end{pmatrix} \tag{5}$$

where z is the distance between the bed surface and the reference level (Figure 1; z is zero in the reference level and increases downward) and c_{f} is the friction coefficient.

The SW equations may also be written in a non-conservative form

$$\frac{\partial \mathbf{U}}{\partial t} + A\frac{\partial \mathbf{U}}{\partial x} + B\frac{\partial \mathbf{U}}{\partial y} = \mathbf{S} + \nabla \mathbf{F}^{\mathrm{d}} \tag{6}$$

where A and B are the Jacobian matrices

$$A = \frac{\partial \mathbf{E}}{\partial \mathbf{U}} = \begin{pmatrix} 0 & 1 & 0 \\ -u^2+c^2 & 2u & 0 \\ -uv & v & u \end{pmatrix}, \quad B = \frac{\partial \mathbf{G}}{\partial \mathbf{U}} = \begin{pmatrix} 0 & 0 & 1 \\ -uv & v & u \\ -v^2+c^2 & 0 & 2v \end{pmatrix} \tag{7}$$

and $c = \sqrt{gh}$ is the wave velocity.

The eigenvalues of A and B are

$$a^1 = u + c, \; a^2 = u, \; a^3 = u - c \quad \text{and} \quad b^1 = v + c, \; b^2 = v, \; b^3 = v - c$$

respectively.

3. NUMERICAL SCHEME

3.1. Finite volume methods on unstructured grids

A finite volume method using triangular grids is used in this paper. The variables are located herein at the geometric centres of the cells, and each triangle represents a control volume. Let $\mathscr{A}$ be the area of a triangle with boundary s. The SW equations are integrated over every control volume

$$\int_t \int_{\mathscr{A}} \left(\frac{\partial \mathbf{U}}{\partial t} + \nabla \mathbf{F} - \mathbf{S} - \nabla \mathbf{F}^{\mathrm{d}} \right) \mathrm{d}\mathscr{A}\, \mathrm{d}t = 0 \tag{8}$$

A high-order time-stepping scheme may be employed to integrate (8) in time. However, for the sake of simplicity and because the discretization of the source term is the main issue, we use here the first-order forward (explicit) Euler time-stepping scheme. This leads to

$$\int_{\mathscr{A}} \left(\frac{\mathbf{U}^{n+1} - \mathbf{U}^n}{\Delta t} + (\nabla \mathbf{F} - \mathbf{S} - \nabla \mathbf{F}^{\mathrm{d}})^n \right) \mathrm{d}\mathscr{A} = 0 \tag{9}$$

where superscript n and $n+1$ refer to the variables at time t_n and t_{n+1}, respectively. The application of Gauss theorem to the diffusive and convective flux integrals gives

$$\int_{\mathscr{A}} (\nabla \mathbf{F} - \nabla \mathbf{F}^{\mathrm{d}})\, \mathrm{d}\mathscr{A} = \oint_s (\mathbf{F} \cdot \mathbf{n} - \mathbf{F}^{\mathrm{d}} \cdot \mathbf{n})\, \mathrm{d}s \tag{10}$$

and the boundary integral is approximated by a summation over the triangle edges

$$\oint_s (\mathbf{F} \cdot \mathbf{n} - \mathbf{F}^{\mathrm{d}} \cdot \mathbf{n})\, \mathrm{d}s = \sum_{k=1}^{3} (\mathbf{F}_k \cdot \mathbf{n}_k - \mathbf{F}_k^{\mathrm{d}} \cdot \mathbf{n}_k) \Delta s_k \tag{11}$$

where k represents the edge index of the triangle and $\mathbf{n}_k$ and Δs_k are the unit outward normal vector and the length of the edge k, respectively. The diffusive fluxes are approximated by a centred scheme

$$\mathbf{F}^{\mathrm{d}} = 0.5(\mathbf{F}_{\mathrm{R}}^{\mathrm{d}} + \mathbf{F}_{\mathrm{L}}^{\mathrm{d}}) \tag{12}$$

A centred scheme for the diffusion term is employed because this scheme is (i) second-order accurate, (ii) economically justified and (iii) easily incorporated in the whole numerical procedure, which is in a flux-based format. Mohammadian *et al.* [10], have shown that scheme (12) for the diffusive fluxes, leads to correct simulation of circulating zones.

The convective fluxes $\mathbf{F}$ are calculated here by a Godunov-type scheme

$$\mathbf{F} = 0.5(\mathbf{F}_{\mathrm{R}} + \mathbf{F}_{\mathrm{L}} - \Delta \mathbf{F}^*) \tag{13}$$

where $\mathbf{F}_{\mathrm{L}} = \mathbf{F}(\mathbf{U}_{\mathrm{L}})$ and $\mathbf{F}_{\mathrm{R}} = \mathbf{F}(\mathbf{U}_{\mathrm{R}})$ are the left and right flux vectors. The subscripts R and L represent the evaluation of the right and left sides of the interface, respectively, and $\Delta \mathbf{F}^*$ is the flux difference based on the Roe's linearization

$$\Delta \mathbf{F}^* = \sum_{k=1}^{3} \tilde{\alpha}^k |\tilde{a}^k| \tilde{\mathbf{e}}^k \tag{14}$$

where $\tilde{a}^k$ and $\tilde{\mathbf{e}}^k$, $k=1,2,3$, are the eigenvalues and the eigenvectors of $\tilde{A}$, respectively. The matrix $\tilde{A}$ represents the Roe's average Jacobian matrix, and it satisfies $\Delta\mathbf{F}=\tilde{A}\Delta\mathbf{U}$ with

$$\tilde{A}=\frac{\partial(\mathbf{F}\cdot\mathbf{n})}{\partial\mathbf{u}}=\begin{pmatrix} 0 & n_x & n_y \\ (\tilde{c}^2-\tilde{u}^2)n_x-\tilde{u}\tilde{v}n_y & 2\tilde{u}n_x+\tilde{v}n_y & \tilde{u}n_y \\ -\tilde{u}\tilde{v}n_x+(\tilde{c}^2-\tilde{v}^2)n_y & \tilde{v}n_x & \tilde{u}n_x+2\tilde{v}n_y \end{pmatrix} \tag{15}$$

where

$$\tilde{u}=\frac{u_{\mathrm{R}}\sqrt{h_{\mathrm{R}}}+u_{\mathrm{L}}\sqrt{h_{\mathrm{L}}}}{\sqrt{h_{\mathrm{R}}}+\sqrt{h_{\mathrm{L}}}},\quad \tilde{v}=\frac{v_{\mathrm{R}}\sqrt{h_{\mathrm{R}}}+v_{\mathrm{L}}\sqrt{h_{\mathrm{L}}}}{\sqrt{h_{\mathrm{R}}}+\sqrt{h_{\mathrm{L}}}},\quad \tilde{c}=\sqrt{g(h_{\mathrm{R}}+h_{\mathrm{L}})/2} \tag{16}$$

In the case of a dry bed problem, $\tilde{c}$ is calculated in the same manner than in (16), and the average velocities are

$$\tilde{u}=\frac{u_{\mathrm{R}}+u_{\mathrm{L}}}{2},\quad \tilde{v}=\frac{u_{\mathrm{R}}+u_{\mathrm{L}}}{2}$$

The eigenvalues of $\tilde{A}$ are simply

$$\tilde{a}^1=\tilde{u}n_x+\tilde{v}n_y+\tilde{c},\quad \tilde{a}^2=\tilde{u}n_x+\tilde{v}n_y,\quad \tilde{a}^3=\tilde{u}n_x+\tilde{v}n_y-\tilde{c} \tag{17}$$

with the corresponding eigenvectors

$$\tilde{\mathbf{e}}^1=\begin{pmatrix} 1 \\ \tilde{u}+\tilde{c}n_x \\ \tilde{v}+\tilde{c}n_y \end{pmatrix},\quad \tilde{\mathbf{e}}^2=\begin{pmatrix} 0 \\ -\tilde{c}n_y \\ \tilde{c}n_x \end{pmatrix},\quad \tilde{\mathbf{e}}^3=\begin{pmatrix} 1 \\ \tilde{u}-\tilde{c}n_x \\ \tilde{v}-\tilde{c}n_y \end{pmatrix} \tag{18}$$

respectively. The coefficients $\tilde{\alpha}^k$, $k=1,2,3$, are computed as

$$\tilde{\alpha}^1=\frac{\Delta h}{2}+\frac{1}{2\tilde{c}}[\Delta(hu)n_x+\Delta(hv)n_y-(\tilde{u}n_x+\tilde{v}n_y)\Delta h] \tag{19}$$

$$\tilde{\alpha}^2=\frac{1}{\tilde{c}}([\Delta(hv)-\tilde{v}\Delta h]n_x-[\Delta(hu)-\tilde{u}\Delta h]n_y) \tag{20}$$

$$\tilde{\alpha}^3=\frac{\Delta h}{2}-\frac{1}{2\tilde{c}}[\Delta(hu)n_x+\Delta(hv)n_y-(\tilde{u}n_x+\tilde{v}n_y)\Delta h] \tag{21}$$

where $\Delta(\cdot)=(\cdot)_{\mathrm{R}}-(\cdot)_{\mathrm{L}}$.

The Roe's method violates the entropy condition in the case of sonic rarefactions (transcritical flows) and it predicts an unphysical jump at the sonic point inside the rarefaction waves, which is physically incorrect. This is because hyperbolic conservation laws admit, for example, rarefaction shocks and compressive shocks. In the SW equations, only the compressive shocks are physically acceptable. The entropy condition is a criterion for selecting the physically meaningful solution, in such cases.

Many methods have been proposed to improve the Roe's method for those flows such as Harten and Hyman [19]. Here, we employ an approach proposed by van Leer *et al.* [20], and

already used by Bradford and Sanders [21]. It consists of modifying the values $|\tilde{a}^k|$, $k=1,2,3$, in (14) when

$$-\frac{\Delta a^k}{2} < \tilde{a}^k < \frac{\Delta a^k}{2} \tag{22}$$

and replacing them by $|\hat{a}^k|$ defined as

$$|\hat{a}^k| = \frac{(\tilde{a}^k)^2}{\Delta a^k} + \frac{\Delta a^k}{4} \tag{23}$$

where

$$\Delta a^k = 4(a_{\mathrm{R}}^k - a_{\mathrm{L}}^k) \tag{24}$$

where, a_{R}^k and a_{L}^k are calculated as in (17), but using $u_{\mathrm{L}}, v_{\mathrm{L}}, c_{\mathrm{L}}$ and $u_{\mathrm{R}}, v_{\mathrm{R}}, c_{\mathrm{R}}$, respectively. Such a simple modification enables the scheme to simulate the transcritical flows correctly.

3.2. *Calculation of derivatives*

The divergence theorem is employed to obtain the derivatives of a scalar variable c on a triangular cell i (shown in Figure 2) as

$$\left(\frac{\partial c}{\partial x}\right)_i = \frac{1}{\mathscr{A}_i}\int_{\mathscr{A}} \frac{\partial c}{\partial x}\,\mathrm{d}\mathscr{A} \approx \frac{c_1\Delta y_1 + c_2\Delta y_2 + c_3\Delta y_3}{\mathscr{A}_i} \tag{25}$$

$$\left(\frac{\partial c}{\partial y}\right)_i = \frac{1}{\mathscr{A}_i}\int_{\mathscr{A}} \frac{\partial c}{\partial y}\,\mathrm{d}\mathscr{A} \approx -\frac{c_1\Delta x_1 + c_2\Delta x_2 + c_3\Delta x_3}{\mathscr{A}_i} \tag{26}$$

where

$$\Delta y_1 = y_3 - y_2, \quad \Delta x_1 = x_3 - x_2, \quad c_1 = (c_1^{\mathrm{L}} + c_1^{\mathrm{R}})/2 \tag{27}$$

$$\Delta y_2 = y_1 - y_3, \quad \Delta x_2 = x_1 - x_3, \quad c_2 = (c_2^{\mathrm{L}} + c_2^{\mathrm{R}})/2 \tag{28}$$

$$\Delta y_3 = y_2 - y_1, \quad \Delta x_3 = x_2 - x_1, \quad c_3 = (c_3^{\mathrm{L}} + c_3^{\mathrm{R}})/2 \tag{29}$$

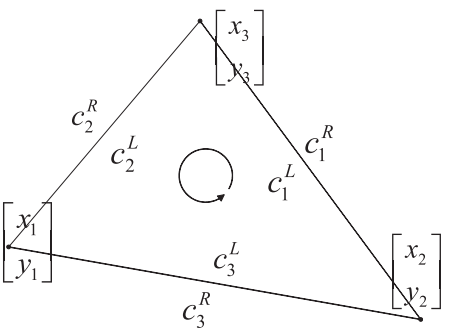

Figure 2. The triangular cell i with the quantities c_j^{R} and c_j^{L} computed at the right (R) and left (L) sides, respectively, at a given face j, $j=1,2,3$. The coordinates (x_j, y_j), $j=1,2,3$, are located at the three vertices of cell i.

The viscous terms are then calculated as

$$\left(vh\frac{\partial u}{\partial x}\right)_i \approx vh_i \frac{u_1\Delta y_1 + u_2\Delta y_2 + u_3\Delta y_3}{\mathscr{A}_i} \tag{30}$$

3.3. Interpolation scheme

The values of the variables at the left and right sides of the interface are needed to compute the numerical fluxes in (12) and (13). Those values may be calculated using a piecewise constant or a piecewise linear interpolation scheme. Because this paper focuses on the discretization of the source terms, for the sake of simplicity, a piecewise constant approach has been employed in all the computations (except where mentioned otherwise). However, the methods presented in the next section to calculate the source terms, also preserve the *C* property when high accurate interpolation schemes are employed (e.g. Appendix A). This is because the *C* property proofs given in Sections 3 and 4 are independent of the method for calculating the variables at the left and right sides of the interface, provided $\Delta h = 0$ at the cell interfaces (which is the case when the surface gradient method employed) in stagnant conditions.

In the surface gradient method [18] the water surface elevation η is interpolated at the cell faces instead of the water depth. Once η_L is calculated, the water depth can be obtained as

$$h_L = \eta_L + z_e \tag{31}$$

where z_e is the distance between the bed surface and the reference level at triangle edge mid-points and is known from topography data. In the case of the stagnant conditions $\eta_L = \eta_R = \eta_0$, where η_0 is the constant water level and using (31) we obtain $h_L = h_R = \eta_0 + z_0$, which leads to $\Delta h = 0$ at the cell faces. This is crucial to guarantee the *C* property proofs given in the next section.

An interpolation procedure (Appendix A) is also needed to calculate the depth integrated discharges *uh* and *vh* at the cell interfaces, and we obtain

$$u_L = \frac{(uh)_L}{h_L} \tag{32}$$

3.4. Computation of bed slope term in variable topographies

As mentioned before, the bed slope term is considered separately in the source term (5). This usually leads to an incompatible discretization of the water surface gradient term ($0.5gh^2$) and the bed slope term and consequently produces an artificial source term in the numerical solution. For example, in complicated topographies with the stagnant initial condition, the water will not remain stagnant [5].

In the following we introduce two methods to overcome this problem.

3.4.1. Method I. Compatible discretization of the bed slope term using a modified water depth. We first explain a simplified version of the method in one dimension. For a cell i, with edges $i+1/2$ and $i-1/2$, and length Δx, the bed slope term is usually approximated as

$$\left(gh\frac{\partial z}{\partial x}\right)_i \approx gh_i \frac{(z_{i+1/2} - z_{i-1/2})}{\Delta x_i} \tag{33}$$

where h_i is the water depth in the cells. Recall z is the distance between the bed surface and the reference level (Figure 1). However, (33) does not satisfy the C property. In order to balance the source terms and the flux gradients, h_i is approximated by $\hat{h}_i$ as

$$\hat{h}_i = \frac{h^{\mathrm{R}}_{i+1/2} + h^{\mathrm{L}}_{i+1/2} + h^{\mathrm{R}}_{i-1/2} + h^{\mathrm{L}}_{i-1/2}}{4} \tag{34}$$

In the case of the stagnant water conditions

$$h^{\mathrm{R}}_{i+1/2} = h^{\mathrm{L}}_{i+1/2} = h_{i+1/2} \tag{35}$$

$$h^{\mathrm{R}}_{i-1/2} = h^{\mathrm{L}}_{i-1/2} = h_{i-1/2} \tag{36}$$

$$\eta^{\mathrm{R}}_{i-1/2} = \eta^{\mathrm{L}}_{i-1/2} = \eta_0 \tag{37}$$

where η_0 is the constant water surface elevation over the domain and hence, $(\Delta h)_k = h^{\mathrm{R}}_k - h^{\mathrm{L}}_k = 0$, with $k = i - 1/2$ and $i + 1/2$. Further, because all velocities are zero (due to the stagnant conditions), we obtain $\Delta \mathbf{F}^* = 0$ and the flux vector is then

$$\mathbf{F} = \begin{pmatrix} 0 \\ 0.5gh^2 \end{pmatrix} \tag{38}$$

In 1D, (9) reduces to (see (10) and (11))

$$\frac{\mathbf{U}^{n+1}_i - \mathbf{U}^n_i}{\Delta t}\Delta x + (\mathbf{F}_{i+1/2} - \mathbf{F}_{i-1/2}) - \mathbf{S}_i \Delta x = 0$$

or

$$\mathbf{U}^{n+1}_i \Delta x = \mathbf{U}^n_i \Delta x - \Delta t(\mathbf{F}_{i+1/2} - \mathbf{F}_{i-1/2}) + \Delta t \mathbf{S}_i \Delta x = 0$$

Therefore, the discretized momentum equation corresponding to cell i (for stagnant conditions) is (see (38))

$$\begin{aligned}(uh)^{n+1}_i \Delta x_i &= (uh)_i \Delta x_i - 0.5g\Delta t(h^2_{i+1/2} - h^2_{i-1/2}) + g\Delta t \frac{h_{i+1/2} + h_{i-1/2}}{2}(z_{i+1/2} - z_{i-1/2}) \\ &= (uh)_i \Delta x_i - 0.5g\Delta t(h_{i+1/2} + h_{i-1/2})(\eta_{i+1/2} - \eta_{i-1/2}) \\ &= (uh)_i \Delta x_i \end{aligned} \tag{39}$$

Hence, the C property holds.

This approach can be extended to arbitrary control volumes. Indeed, following (25), the bed slope term in a cell i (Figure 3) is discretized as

$$\left(gh\frac{\partial z}{\partial x}\right)_i \approx gh_i \left(\frac{\partial z}{\partial x}\right)_i \approx gh_i \left(\frac{z_1 \Delta y_1 + z_2 \Delta y_2 + z_3 \Delta y_3}{\mathscr{A}_i}\right) \tag{40}$$

where Δy_3 is replaced by $\Delta y_3 = -(\Delta y_1 + \Delta y_2)$ and this leads to

$$\left(gh\frac{\partial z}{\partial x}\right)_i = \frac{g}{\mathscr{A}_i}\left(\underbrace{h_i \Delta y_1 (z_1 - z_3)}_{part\ 1} + \underbrace{h_i \Delta y_2 (z_2 - z_3)}_{part\ 2}\right) \tag{41}$$

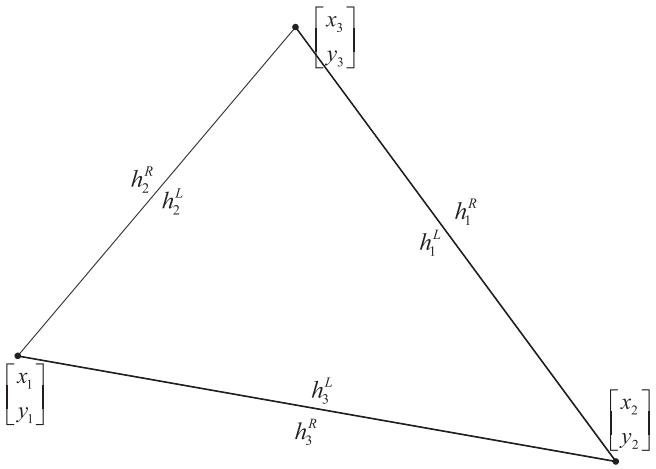

Figure 3. The triangular cell i with the quantities h_j^{R} and h_j^{L} computed at the right (R) and left (L) sides, respectively, at a given face j, $j=1,2,3$. The coordinates (x_j, y_j), $j=1,2,3$, are located at the three vertices of cell i.

Again, (41) does not satisfy the C property because there is still an imbalance between the bed slope and the flux terms. In order to reach the balance, the right-hand side of (41) is expressed in two parts (parts 1 and 2). Following the same procedure than in (33) and (34), we replace h_i by

$$\hat{h}_{1-3} = \frac{h_1^{\mathrm{R}} + h_1^{\mathrm{L}} + h_3^{\mathrm{R}} + h_3^{\mathrm{L}}}{4} \tag{42}$$

and

$$\hat{h}_{2-3} = \frac{h_2^{\mathrm{R}} + h_2^{\mathrm{L}} + h_3^{\mathrm{R}} + h_3^{\mathrm{L}}}{4} \tag{43}$$

in parts 1 and 2 of (41), respectively (Figure 3), and this leads to

$$\left(gh\frac{\partial z}{\partial x}\right)_i = \frac{g}{\mathscr{A}_i}\left(\frac{h_1^{\mathrm{R}} + h_1^{\mathrm{L}} + h_2^{\mathrm{R}} + h_2^{\mathrm{L}}}{4}\Delta y_1(z_1 - z_3) + \frac{h_2^{\mathrm{R}} + h_2^{\mathrm{L}} + h_3^{\mathrm{R}} + h_3^{\mathrm{L}}}{4}\Delta y_2(z_2 - z_3)\right) \tag{44}$$

Proposition 1
The numerical scheme presented in Sections 3.1–3.3, satisfies the C property with (44).

Proof
In the case of stagnant water conditions we have

$$h_1^{\mathrm{R}} = h_1^{\mathrm{L}} = h_1 \tag{45}$$

$$h_2^{\mathrm{R}} = h_2^{\mathrm{L}} = h_2 \tag{46}$$

$$h_3^{\mathrm{R}} = h_3^{\mathrm{L}} = h_3 \tag{47}$$

$$\eta_1 = \eta_2 = \eta_3 = \eta_0 \tag{48}$$

and the corresponding term of $\int_{\mathscr{A}} \nabla \mathbf{F}\, \mathrm{d}\mathscr{A}$ in (9) for the x-momentum equation, reduces to $\int_{\mathscr{A}} [\partial(0.5gh^2)/\partial x]\, \mathrm{d}\mathscr{A}$. By using the divergence theorem as in (10), it is numerically approximated as (see (11)) $0.5g(h_1^2 \Delta y_1 + h_2^2 \Delta y_2 + h_3^2 \Delta y_3)$. Therefore, the discretized momentum equation corresponding to cell i is

$$\begin{aligned}
(uh)_i^{n+1} \mathscr{A}_i &= (uh)_i \mathscr{A}_i - 0.5g\Delta t(h_1^2 \Delta y_1 + h_2^2 \Delta y_2 + h_3^2 \Delta y_3) \\
&\quad + g\Delta t \left(\frac{h_1 + h_3}{2} \Delta y_1 (z_1 - z_3) + \frac{h_2 + h_3}{2} \Delta y_2 (z_2 - z_3) \right) \\
&= (uh)_i \mathscr{A}_i - \frac{g\Delta t}{4} ((h_2 + h_1)(h_2 - z_2 - h_1 + z_1) \Delta y_1 \\
&\quad + (h_3 + h_2)(h_3 - z_3 - h_2 + z_2) \Delta y_2) \\
&= (uh)_i \mathscr{A}_i - \frac{g\Delta t}{4} ((h_2 + h_1)(\eta_2 - \eta_1) \Delta y_1 + (h_3 + h_2)(\eta_3 - \eta_2) \Delta y_2) \\
&= (uh)_i \mathscr{A}_i
\end{aligned} \tag{49}$$

The C property thus holds. The extension of the present method for an arbitrary control volume with m edges is straightforward by considering

$$\sum_{k=1}^{m} \Delta y_k = 0 \tag{50}$$

Therefore, (40) and (41) could be generalized as

$$\left(gh \frac{\partial z}{\partial x} \right)_i \approx gh_i \left(\frac{\partial z}{\partial x} \right)_i \approx gh_i \left(\frac{\sum_{k=1}^{m} z_k \Delta y_k}{\mathscr{A}_i} \right)$$

with $\Delta y_m = -\sum_{k=1}^{m-1} \Delta y_k$ is deduced from (50) and this leads to

$$\left(gh \frac{\partial z}{\partial x} \right)_i = \frac{g}{\mathscr{A}_i} \left(\sum_{k=1}^{m-1} \hat{h}_k \Delta y_k (z_k - z_m) \right)$$

with

$$\hat{h}_k = \frac{h_k^{\mathrm{R}} + h_k^{\mathrm{L}} + h_m^{\mathrm{R}} + h_m^{\mathrm{L}}}{4}$$

The proof of Proposition 1 is then generalized in a similar manner. □

3.4.2. Method II. Considering different components of the bed slope term separately. In method I, two different approximations (42) and (43) have been used to approximate the depth inside a given triangular cell in order to balance the source and the flux gradient terms. For general control volumes having more than three edges (such as quadrilaterals) the accuracy of method I may be decreased in the case of stretched cells. This problem motivates the introduction of method II in which the source and the flux gradient terms are inherently balanced by considering different components of the bed slope term separately.

Here, the bed slope term is written as

$$\begin{aligned} gh\frac{\partial z}{\partial x} &= g\frac{\partial(hz)}{\partial x} - gz\frac{\partial h}{\partial x} \\ &= 0.5g\frac{\partial(hz)}{\partial x} + 0.5g\frac{\partial(hz)}{\partial x} - gz\frac{\partial h}{\partial x} \\ &= \underbrace{0.5g\frac{\partial(hz)}{\partial x}}_{B_1} + \underbrace{0.5gh\frac{\partial z}{\partial x}}_{B_2} - \underbrace{0.5gz\frac{\partial h}{\partial x}}_{B_3} \end{aligned} \tag{51}$$

where

$$B_1 = \frac{0.5g}{\mathscr{A}_i}\left(\frac{h_1^{\mathrm{L}} + h_1^{\mathrm{R}}}{2} z_1 \Delta y_1 + \frac{h_2^{\mathrm{L}} + h_2^{\mathrm{R}}}{2} z_2 \Delta y_2 + \frac{h_3^{\mathrm{L}} + h_3^{\mathrm{R}}}{2} z_3 \Delta y_3\right) \tag{52}$$

$$B_2 = \frac{0.5gh_i}{\mathscr{A}_i}(z_1 \Delta y_1 + z_2 \Delta y_2 + z_3 \Delta y_3) \tag{53}$$

$$B_3 = \frac{0.5gz_i}{\mathscr{A}_i}\left(\frac{h_1^{\mathrm{L}} + h_1^{\mathrm{R}}}{2} \Delta y_1 + \frac{h_2^{\mathrm{L}} + h_2^{\mathrm{R}}}{2} \Delta y_2 + \frac{h_3^{\mathrm{L}} + h_3^{\mathrm{R}}}{2} \Delta y_3\right) \tag{54}$$

In the case of a horizontal bed, B_1 and B_3 cancel each other and B_2 is equal to zero.

Proposition 2
The numerical scheme presented in Sections 3.1–3.3, satisfies the C property with (51)–(54).

Proof
The stagnant condition leads to

$$\begin{aligned} (uh)_i^{n+1}\mathscr{A}_i &= (uh)_i\mathscr{A}_i - 0.5g\Delta t(h_1^2\Delta y_1 + h_2^2\Delta y_2 + h_3^2\Delta y_3) + \Delta t\mathscr{A}_i(B_1 + B_2 + B_3) \\ &= (uh)_i\mathscr{A}_i - 0.5g\Delta t(h_1(h_1 - z_1)\Delta y_1 + h_2(h_2 - z_2)\Delta y_2 \\ &\quad + h_3(h_3 - z_3)\Delta y_3) + \Delta t\mathscr{A}_i(B_2 - B_3) \\ &= (uh)_i\mathscr{A}_i - 0.5g\eta_0\Delta t(h_1\Delta y_1 + h_2\Delta y_2 + h_3\Delta y_3) + \Delta t\mathscr{A}_i(B_2 - B_3) \end{aligned} \tag{55}$$

and

$$\begin{aligned} (B_2 - B_3)\mathscr{A}_i &= 0.5gh_i((h_1 - \eta_1)\Delta y_1 + (h_2 - \eta_2)\Delta y_2 + (h_3 - \eta_3)\Delta y_3) \\ &\quad -0.5g\Delta tz_i(h_1\Delta y_1 + h_2\Delta y_2 + h_3\Delta y_3) \\ &= 0.5g(h_i - z_i)(h_1\Delta y_1 + h_2\Delta y_2 + h_3\Delta y_3) + 0.5g\Delta t\eta_0 h_i(\Delta y_1 + \Delta y_2 + \Delta y_3) \\ &= 0.5g\eta_0(h_1\Delta y_1 + h_2\Delta y_2 + h_3\Delta y_3) \\ &= 0.5g\eta_0(h_1\Delta y_1 + h_2\Delta y_2 + h_3\Delta y_3) \end{aligned} \tag{56}$$

Substituting (56) in (55) we obtain

$$(uh)_i^{n+1}\mathscr{A}_i = (uh)_i\mathscr{A}_i \tag{57}$$

Hence, the C property holds. This proof is directly generalized in the case of an arbitrary control volume having more than three edges, by adding the corresponding terms to (52)–(54). □

3.5. Computational modelling of wetting and drying fronts

It is generally accepted that the wetting–drying simulation is very hard [22]. This is particularly the case in real applications with complicated topographies using unstructured grids. Therefore, an algorithm to treat wetting and drying fronts is generally needed.

In this paper, if the water depth in a cell is less than a specified value $h_{\min}$, then this cell is considered as a dry cell. In such a cell all *outward* fluxes and also the bed slope and friction source terms are set to zero. Inward fluxes are always active, as a mechanism for wetting the dry cells.

3.6. Boundary conditions

In order to treat the boundary conditions, the variables at boundary faces are imposed as following:

Subcritical flow: inflow: two external conditions and outflow: one external condition.
Supercritical flow: inflow: three external conditions and outflow: none.
Solid walls: velocity components are set zero.

All remaining conditions may be calculated based on the characteristics theory, i.e. by using the information carried out by the outgoing bicharacteristics (the Riemann invariants). However, in most practical cases those may be simply set to the corresponding values of the adjacent inner cells.

4. NUMERICAL RESULTS

In order to study the performance of the numerical scheme, some tests have been performed herein for variable topographies. In all figures and tables, the SI system has been used, i.e. the water depth and the water surface elevation are in meters (m) and the water discharge is in $m^3\,s^{-1}$. Note that methods I and II present the same results in the following tests and no visible difference is observed.

4.1. Tidal wave flow over an irregular topography

The topography for this case [23] is defined in Table I and graphically represented in Figure 4. The initial conditions write

$$h(x,0) = H(x) \tag{58}$$

$$u(x,0) = 0 \tag{59}$$

Table I. Topography for an irregular bed.

x (m)	0	50	100	150	250	300	350	400	425	435	450	475	500	505
z (m)	0	20	2.5	5	5	3	5	5	7.5	8	9	9	9.1	9
x (m)	530	550	565	575	600	650	700	750	800	820	900	950	1000	1500
z (m)	9	6	5.5	5.5	5	4	3	3	2.3	2	1.2	0.4	0	0

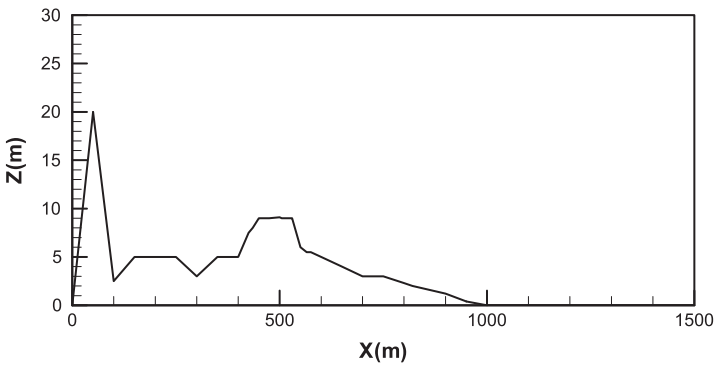

Figure 4. Topography for an irregular bed.

with

$$L = 1500\,\text{m}, \quad H(x) = H(0) - z(x), \quad H(0) = 16\,\text{m}$$

The boundary conditions are

$$h(0,t) = H(0) + 4 - 4\sin\left[\pi\left(\frac{4t}{86\,400} + \frac{1}{2}\right)\right] \tag{60}$$

$$u(L,t) = 0 \tag{61}$$

For this test, Bermudez and Vazquez-Cendon [5] derived the following 'asymptotic' unsteady solution by writing the equations in dimensionless form and asymptotic expansions in terms of the Froude number.

$$h(x,t) = H(x) + 4 - 4\sin\left[\pi\left(\frac{4t}{86\,400} + \frac{1}{2}\right)\right] \tag{62}$$

$$u(x,t) = \frac{(x-L)\pi}{5400h(x,t)}\cos\left[\pi\left(\frac{4t}{86\,400} + \frac{1}{2}\right)\right] \tag{63}$$

At time $t = 10\,800$ s, the numerical results using a CFL number of 0.63 and 100 grid points are shown in Figure 5 (left). The results of the original scheme, i.e. using (40), (instead of the proposed method I or II, i.e. (34) or (51), respectively), are also presented in Figure 5 (right). In this test case, the original scheme shows a high level of oscillations due to the irregular

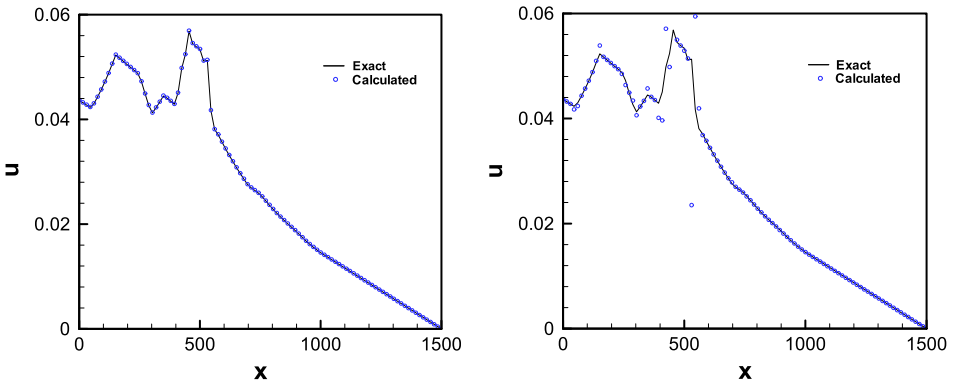

Figure 5. Tidal wave flow over an irregular bed, velocity: Present method (left) and the original scheme (right).

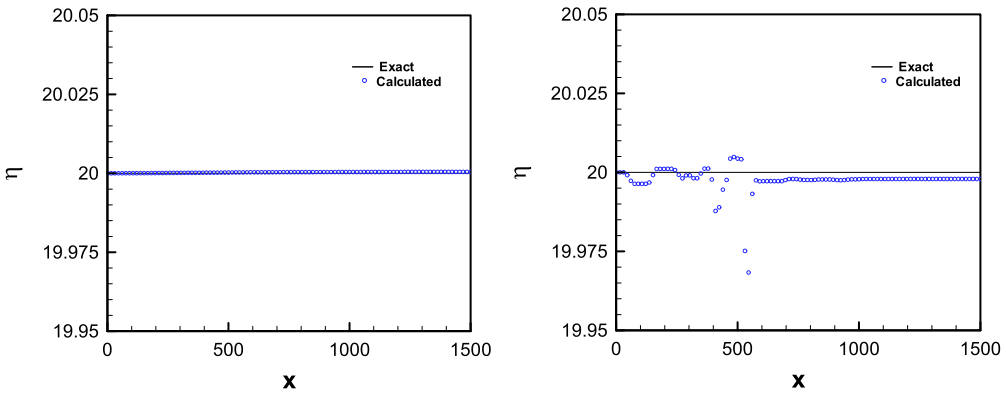

Figure 6. Tidal wave flow over an irregular bed, water surface elevation: Present method (left) and the original scheme (right).

topography which cannot be handled because the imbalance between the source and flux terms, while a considerable improvement is observed with method I or II. The numerical results for water surface are shown in Figure 6, which again show the performance of the proposed methods. Finally, the numerical result of velocity and water surface elevation obtained by the proposed method and the original scheme for the stagnant conditions are presented for $t = 40$ s in Figures 7 and 8, respectively. As, shown, contrary to the original scheme, the proposed method can preserve the stagnant conditions.

4.2. A surge crossing a step

Here we consider a surge crossing a step. A channel of length 10 000 m is used with a step of height 2 m, located at the middle of the channel (Figure 9). This test case has been previously studied by Hu *et al.* [24] who replaced the step by a steep bed slope. A grid of 400 uniform cells is used here.

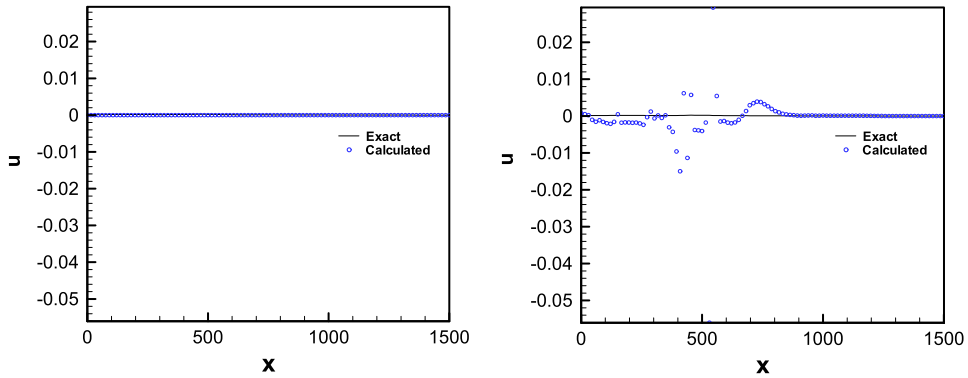

Figure 7. Stagnant condition over an irregular bed, velocity: Present method (left) and the original scheme (right).

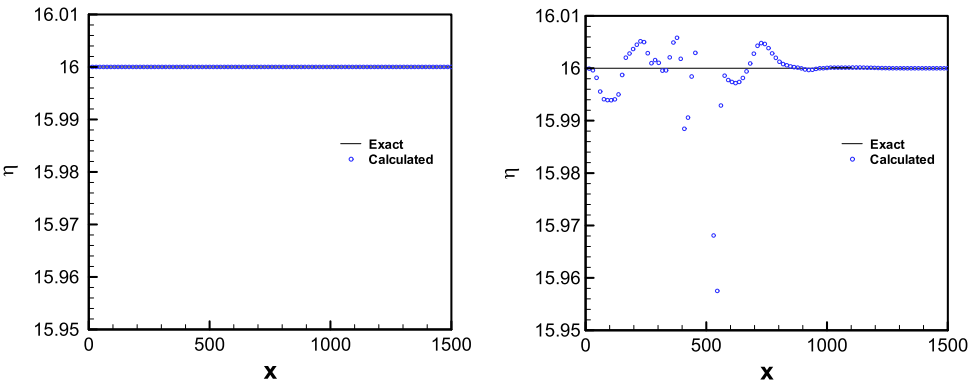

Figure 8. Stagnant condition over an irregular bed, water surface: Present method (left) and the original scheme (right).

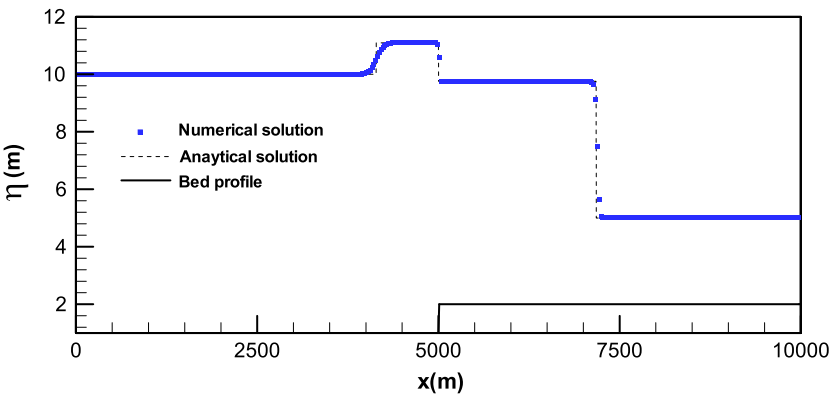

Figure 9. Surge crossing a step: computed water surface at $t = 600$ s.

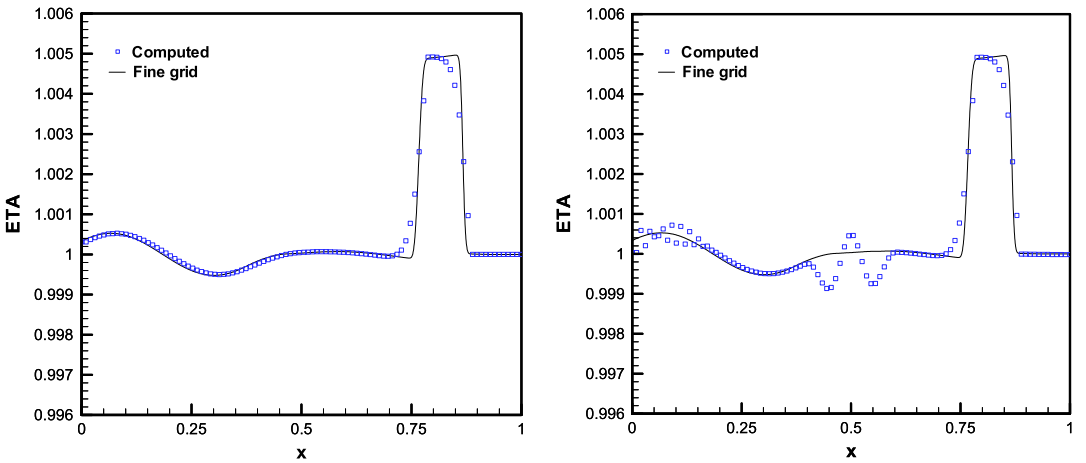

Figure 10. Computed water surface level at $t = 0.7$ s with $\varepsilon = 0.01$: Present method (left) and the original scheme (right).

The initial water surface is 5 m in the channel, the water depth at the upstream end is 10 m, and the velocity of the surge at the entrance is defined as [24]

$$u(0,t) = (\eta_u - \eta_d)\sqrt{\frac{g(\eta_u + \eta_d)}{2\eta_u \eta_d}} \tag{64}$$

where $\eta_u = 10$ m and $\eta_d = 5$ m.

In Figure 9, the numerical results obtained using method I or II are compared with the analytical solution [24]. They show the ability of the model in simulating surges over discontinuous bed profiles.

4.3. *One-dimensional, small perturbation of a steady-state solution*

A small perturbation of a steady-state solution, proposed by Leveque [8], is a challenging test for evaluating the performance of numerical schemes over variable topographies. A channel of length 1.0 m is considered with the following topography

$$z(x,y) = \begin{cases} -0.8\exp(-5(x-0.9)^2 - 50(y-0.5)^2) & \text{for } |x-0.5| \leqslant 0.1 \\ 0.0 & \text{otherwise} \end{cases} \tag{65}$$

with a zero initial flow velocity and a surface profile defined as

$$\eta(x,y) = \begin{cases} 1.0 + \varepsilon & \text{for } 0.1 < x < 0.2 \\ 1.0 & \text{otherwise} \end{cases} \tag{66}$$

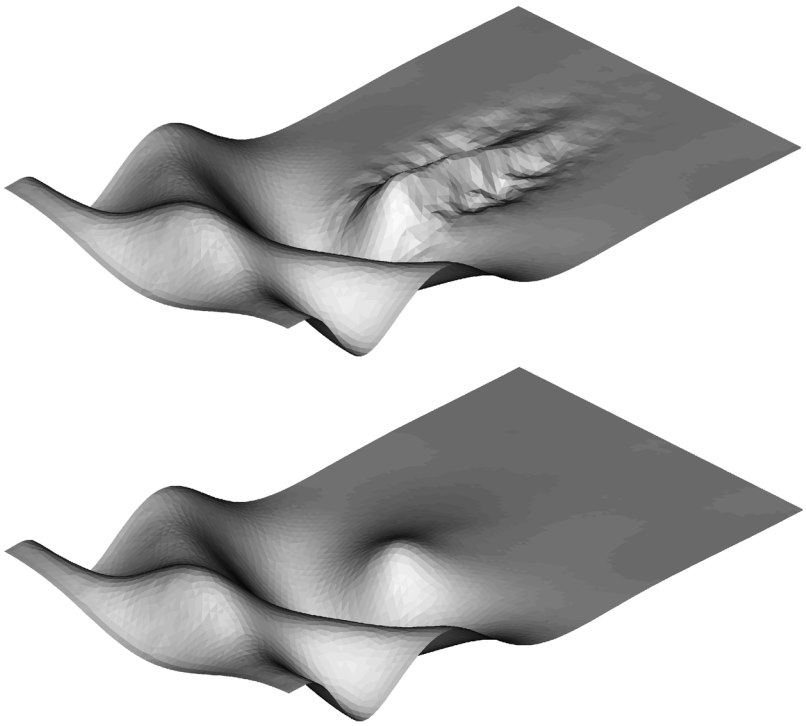

Figure 11. Computed water surface level at $t = 1.8\,\mathrm{s}$ with $\varepsilon = 0.01$: Present method (bottom) and the original scheme (top).

Following Leveque [8], $\varepsilon = 0.01\,\mathrm{m}$ and the reduced gravitational acceleration is $g = 1\,\mathrm{m^2\,s^{-1}}$. Here, a CFL number of 0.99 is used. The numerical results obtained on a very fine grid (1500 nodes), using method I or II, are used as reference solutions in the absence of an analytical one. On a grid of 100 nodes, the results obtained with method I or II and the original scheme are compared with the reference solution in Figure 10. This case is a challenging one, and most existing schemes have used considerably more grid points than here (such as 600 in Reference [25]). As shown in Figure 10, method I or II can capture the quasi-steady solutions quite well, and a considerable improvement is observed compared to the original scheme.

4.4. Two-dimensional, small perturbation of a steady-state solution

In this test case [8], the SW equations are solved in a domain $[0, 2] \times [0, 1]$, and the bottom surface is an elliptical shaped hump

$$z(x, y) = -0.8 \exp(-5(x - 0.9)^2 - 50(y - 0.5)^2) \tag{67}$$

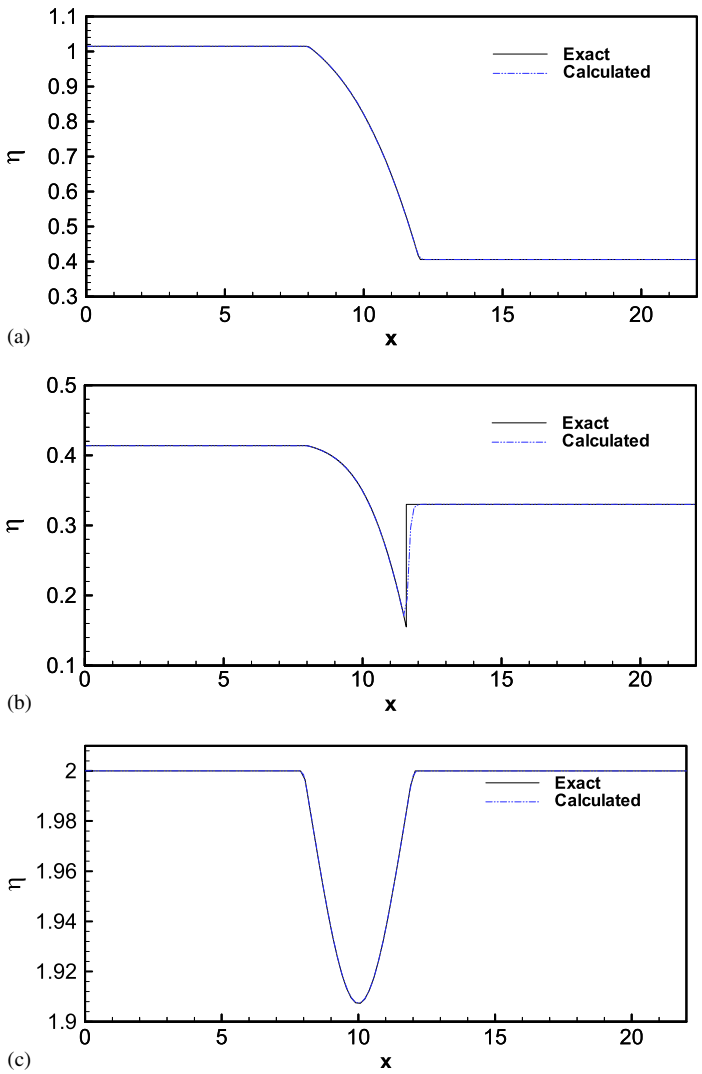

Figure 12. (a) Steady transcritical flow over a bump without a shock: Water surface elevation; (b) Steady transcritical flow over a bump with a shock: Water surface elevation; and (c) Steady subcritical flow over a bump: Water surface elevation.

The water surface is initially flat with $h(x, y) = 1$ except for $0.05 < x < 0.15$, where $h(x, y) = 1.01$ m. An unstructured grid with 12 344 triangular cells and a CFL number of 0.6 is used for this test. Figure 11 displays the right-going disturbance at $t = 1.8$ s as it propagates past the hump. This shows the ability of the model in simulating 2D-problems with variable topographies without producing numerical oscillations.

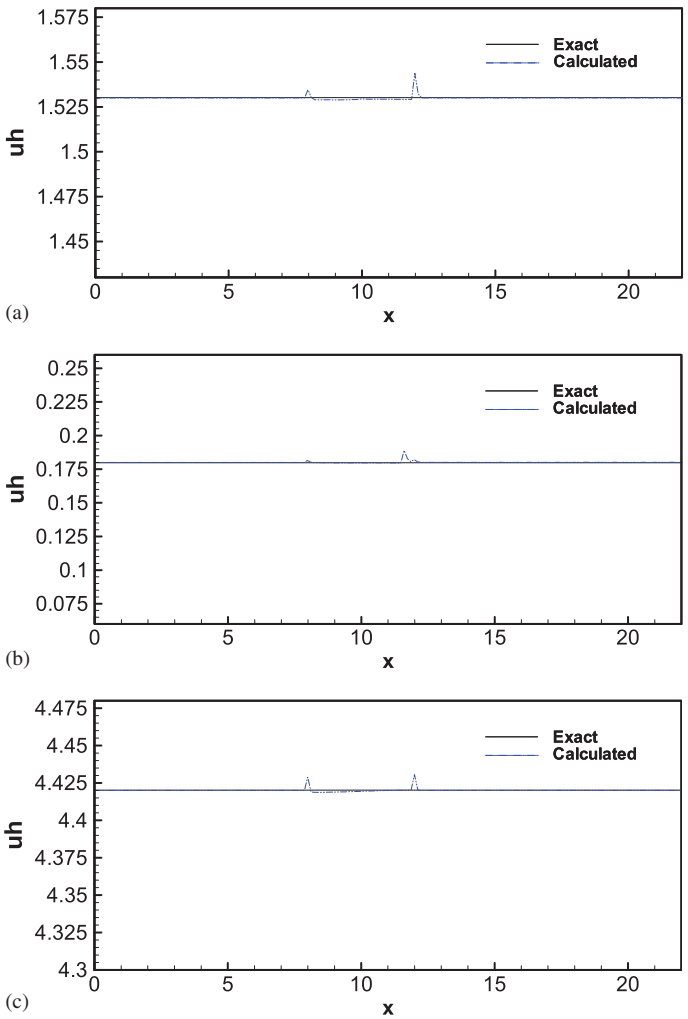

Figure 13. (a) Water discharge in steady transcritical flow over a bump without a shock; (b) Water discharge in steady transcritical flow over a bump with a shock; and (c) Water discharge in steady subcritical flow over a bump without a shock.

4.5. *Steady flow over a bump*

The topography is now defined [23] as

$$z(x) = \begin{cases} 0.2 - 0.05(x-10)^2 & \text{if } 8 < x < 12 \\ 0 & \text{otherwise} \end{cases} \tag{68}$$

Depending on the initial and boundary conditions, the flow may be subcritical, transcritical (with or without a steady shock), or supercritical. The analytical solution of this problem

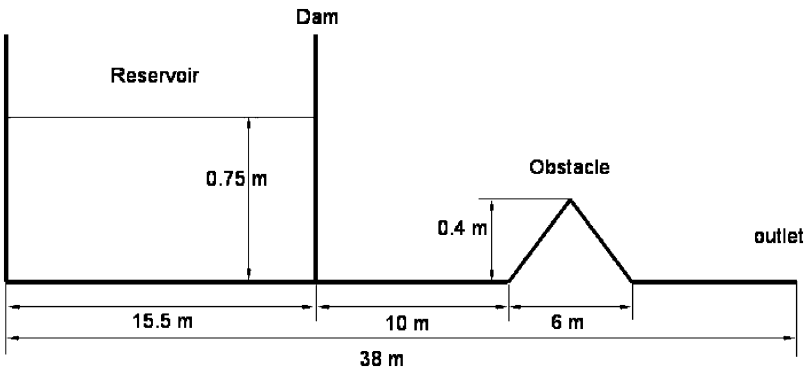

Figure 14. Geometry of the experimental model in the simulation of a dam break and advance over a triangular obstacle.

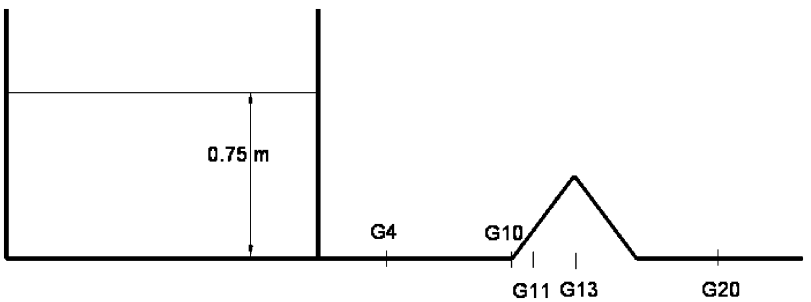

Figure 15. Location of the gauging points in the experimental model for the simulation of a dam break and advance over a triangular obstacle.

is given in Reference [23]. An unstructured grid of average triangle edges equal to 0.075 m was used in all computations. A high-order accurate interpolation scheme (Appendix A) was employed in this test case.

Three different cases are considered below by imposing downstream and upstream boundary conditions for the water level (h) and the discharge (uh), respectively:

(i) *Transcritical flow without shock*: $h = 0.66\,\mathrm{m}$ only when the flow is subcritical and $uh = 1.53\,\mathrm{m^3\,h^{-1}}$.
(ii) *Transcritical flow with shock*: $h = 0.33\,\mathrm{m}$ and $uh = 0.18\,\mathrm{m^3\,h^{-1}}$.
(iii) *Subcritical flow*: $= 2\,\mathrm{m}$ and $uh = 4.42\,\mathrm{m^3\,h^{-1}}$.

The surface profiles are plotted in Figures 12(a)–(c) for method I or II, and they show good agreements with the analytical solutions. The computed discharges are also compared in Figures 13(a)–(c) with the analytical ones, which show a low level of numerical oscillations. It should be mentioned that such a level of numerical oscillations is also present in most existing schemes. This is because the C property, although widely accepted in the literature as a good measure to test the ability of numerical schemes in the presence of real

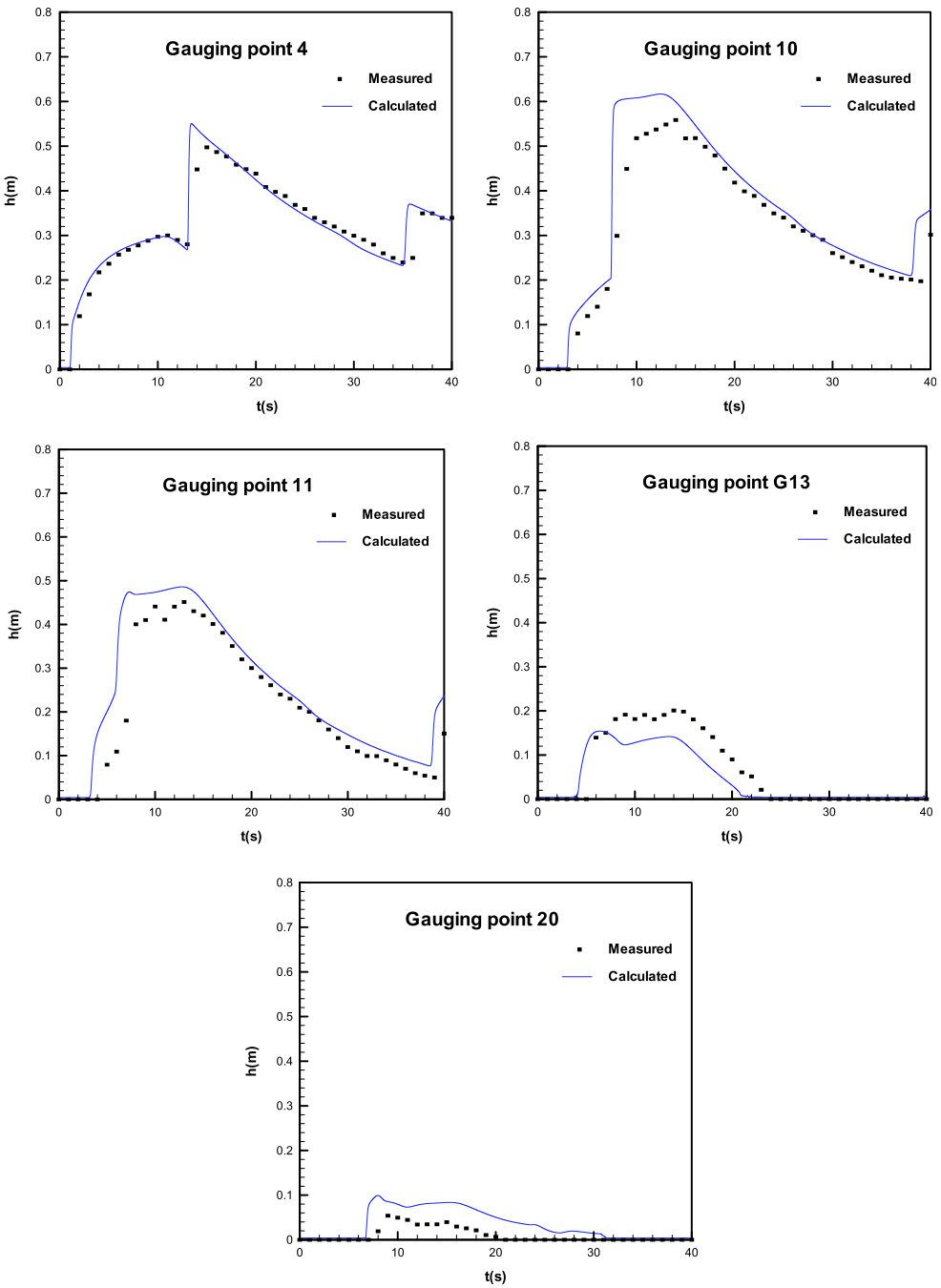

Figure 16. Time evolution during 40 s of the water depth measured and computed at gauging points: G4, G10, G11, G13 and G20 in the simulation of a dam break and advance over a triangular obstacle. Points stand for experimental measures and solid line for numerical results.

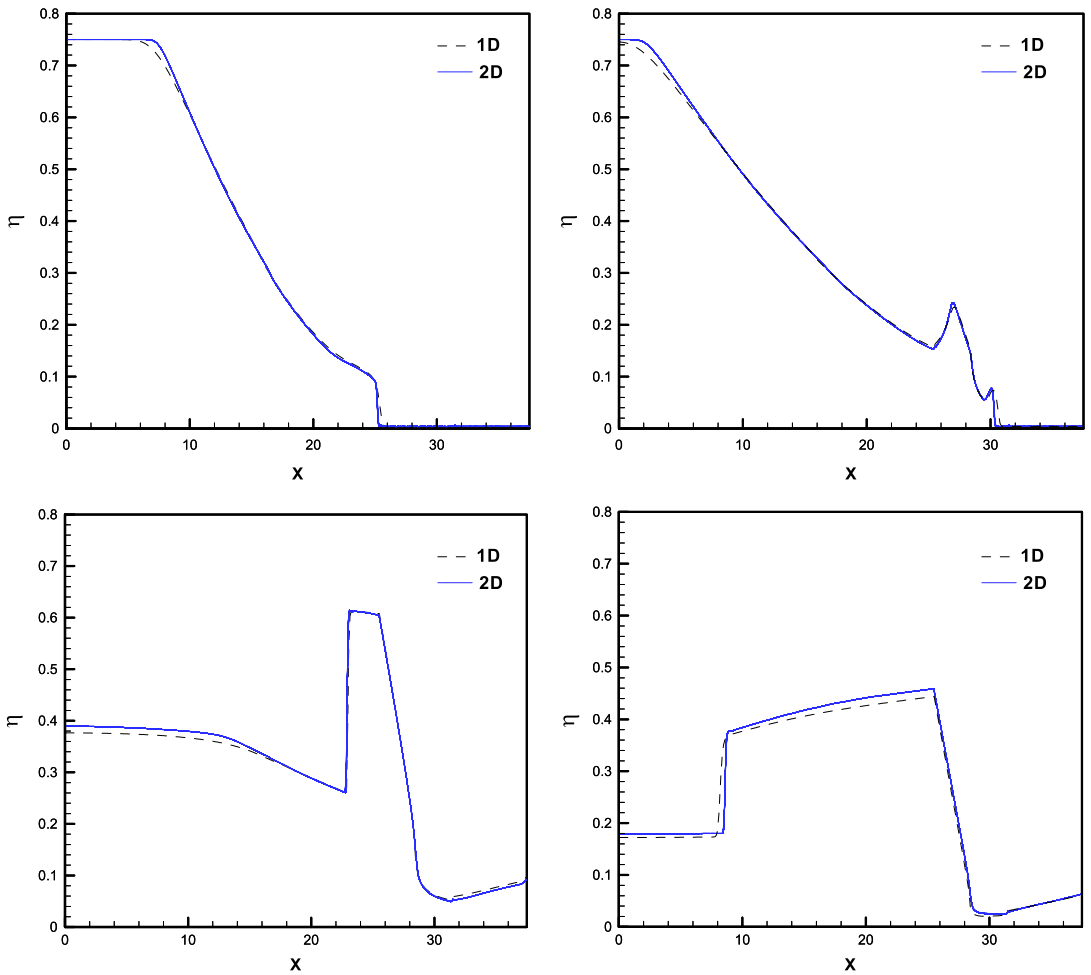

Figure 17. Numerical results obtained with a 1D and a 2D scheme on the water depth profiles along the channel at times: $T = 3, 5, 10$ and 20 s in the simulation of a dam break and advance over a triangular obstacle.

topographies, does not guarantee that the steady-state conditions with non-zero discharge is well captured.

4.6. Dam break and advance over a triangular obstacle

In this test case, evolution of a dam-break wave over a triangular obstacle is examined. The channel geometry is presented in Figure 14. The physical model combines a reservoir connected to a rectangular channel. The length of the entire model is 22.5 m. The dam is situated at $x = 15.5$ m. A triangular obstacle (6 m long, 0.4 m high) is situated 13 m downstream the dam over the bed of the channel. The slopes of the obstacle are symmetric. The initial conditions considered are 0.75 m of water depth in the reservoir and dry bed in the rest of

the channel. The fixed boundaries are solid walls except for the free outlet. The Manning roughness coefficient is 0.0125 for the bed and 0.011 for the vertical walls of the rectangular channel, values supplied by the experimentalists from a steady flow test case. Gauging points are located: G4 at 4 m, G10 at 10 m, G11 at 11 m, G13 at 13 m and G20 at 20 m as shown in Figure 15. Experimental data are reported in Reference [27] which are obtained from the Recherches Hydrauliques Lab. Chatelet together with the University of Bruxelles (Belgium) under the supervision of J.M. Hiver.

A minimum wet depth of $h_{\min} = 0.004$ m was considered in the numerical calculations. Sensitivity analysis with the 1D model showed that reducing the $h_{\min}$ has minor effects on the numerical results. The predicted and measured water depth time evolutions during 40 s at the gauging points are presented in Figure 16 which shows a satisfactory concordance. The water depth and the arrival time of the wave are predicted well at G4, G10 and G11 which are located before the obstacle. It can be observed that. Moreover, the transition from wet to dry is correctly predicted at point G13, which is a critical point since it is located at the vertex of. At the last point (G20) a little disagreement between measures and numerical results is observed but the amount of water is insignificant. The same feature is also observed by Brufau *et al.* [27] and may be related to vertical non-hydrostatic motions that are ignored in SW equations.

Finally, Figure 17 compares the numerical results obtained for the water depth at different times from the 1D and 2D numerical schemes. As it can be seen in Figure 17, results of two models coincide, which is expected due to the nearly 1D feature of the flow (i.e. lateral changes are negligible) and this shows the coherence of both models.

5. CONCLUSION

Two efficient methods have been proposed to treat the source terms and to satisfy the compatibility property on unstructured grids. In the proposed methods, it is not necessary to perform extra upwinding or Riemann solution for the source terms. Contrary to many available schemes, our approach can be easily implemented on unstructured grids and it takes advantage of being flexible for irregular boundaries and local mesh refinement. Numerical results indicated that the proposed methods accurately simulate sub, super and transcritical flows in complicated topographies and also the circulating flows.

APPENDIX A: INTERPOLATION SCHEME

In the present cell-centred scheme, the variables are located at the triangle barycentres and the values of the variables at the left and right sides of the interface are needed to compute the numerical fluxes and source terms. Consider two adjacent triangles as shown in Figure A1.

A first-order approximation of η, uh, vh at left and right-hand side of the cell interfaces is simply equal to their values in the corresponding cell. For example,

$$\eta_{\mathrm{L}} = \eta_{b_{\mathrm{L}}}$$

$$(uh)_{\mathrm{L}} = (uh)_{b_{\mathrm{L}}}$$

$$(vh)_{\mathrm{L}} = (vh)_{b_{\mathrm{L}}}$$

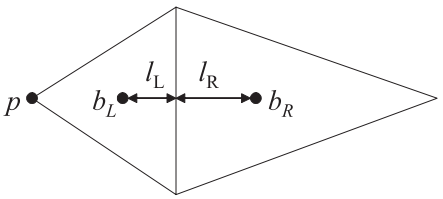

Figure A1. Two adjacent triangles with barycentres b_L and b_R, where l_L and l_R are the lengths between the mid-side node of the common face and b_L and b_R, respectively.

Various methods have been proposed for developing higher-order accurate interpolation schemes. Here, some details of a high-order monotonic interpolation method, is described.

For a scalar variable such as η, the interface values η_L and η_R (on the left and right sides of a given face, respectively) are calculated by the κ scheme [28]. For example, η_L is calculated as

$$\eta_L = \eta_{b_L} + \frac{s}{4}[(1-\kappa s)\Delta_- + (1+\kappa s)\Delta_+] \tag{A1}$$

$$\Delta_- = (\eta_{b_L} - \eta_p), \quad \Delta_+ = [2l_L/(l_L + l_R)](\eta_{b_R} - \eta_{b_L}) \tag{A2}$$

where $\kappa = -1$ leads to an upwind scheme, $\kappa = 0$ to the Fromm scheme, $\kappa = 1$ to a central scheme and $\kappa = 1/3$ to a third-order scheme (in 1D).

The slope limiter s, is chosen according to Battina [28]

$$s = \frac{2\Delta_-\Delta_+ + \varepsilon}{\Delta_-^2 + \Delta_+^2 + \varepsilon} \tag{A3}$$

where ε is a very small number for avoiding division by zero in the regions of mild slope. The interface values of uh and vh are calculated similarly.

ACKNOWLEDGEMENTS

Authors are supported by grants from the Natural Science and Engineering Council (NSERC) and the Fonds Québécois de la Recherche sur la Nature et les Technologies (FQRNT).

REFERENCES

1. Glaister P. Approximate Riemann solutions of the shallow-water equations. *Journal of Hydraulic Research* 1988; **26**(3):293–306.
2. Fenemma R, Chaudhry M. Simulation of one-dimensional dam-break flows. *Journal of Hydraulic Research* 1987; **25**(1):41–51.
3. Zhao D, Shen HW, Tabios GQ III, Lai JS, Tan WY. Finite-volume two-dimensional unsteady-flow model for river basins. *Journal of Hydraulic Engineering* (ASCE) 1994; **120**(7):863–883.
4. Mingham CG, Causon DM. High resolution finite-volume method for shallow-water equation flows. *Journal of Hydraulic Engineering* (ASCE) 1998; **124**:605–614.
5. Bermudez A, Vazquez-Cendon ME. Upwind methods for hyperbolic conservation laws with source terms. *Computers and Fluids* 1994; **23**:1049–1071.
6. Vazquez-Cendon ME. Improved treatment of source terms in upwind schemes for the shallow-water equations in channels with irregular geometry. *Journal of Computational Physics* 1999; **43**(2):357–372.

7. Hubbard ME, Garcia-Navarro P. Balancing source terms and flux gradients in finite volume schemes. In *Godunov Methods*: *Theory and Applications*, Toro EF (ed.). Kluwer Academic Publishers: New York, 2001; 447–483.
8. LeVeque RJ. Balancing source terms and flux gradients in high-resolution Godunov methods. *Journal of Computational Physics* 1998; **146**:346–365.
9. Kurganov A, Levy D. Central-upwind schemes for the Saint-Venant system. *Mathematical Modeling and Numerical Analysis* 2002; **36**:397–425.
10. Mohammadian A, Le Roux DY, Tajrishi M, Mazaheri K. A mass conservative scheme for simulating shallow flows over variable topographies using unstructured grid. *Advances in Water Resources* 2005; **28**(5):429–539.
11. Alcrudo F, Benkhaldoun F. Exact solutions to the Riemann problem of the shallow-water equations with a bottom step. *Computers and Fluids* 2001; **30**:643–671.
12. Vukovic S, Sopta L. ENO and WENO schemes with the exact conservation property for one-dimensional shallow-water equations. *Journal of Computational Physics* 2002; **179**:593–621.
13. Jin S. Steady-state capturing method for hyperbolic systems with geometrical source terms. *Mathematical Modelling and Numerical Analysis* 2001; **35**:631–646.
14. Xu K. A well-balanced gas-kinetic scheme for the shallow-water equations with source terms. *Journal of Computational Physics* 2002; **178**:533–562.
15. Rogers BD, Borthwick AL, Taylor PH. Mathematical balancing of flux gradient and source terms prior to using Roe's approximate Riemann solver volume. *Journal of Computational Physics* 2003; **192**(2):422–451.
16. Nujic M. Efficient implementation of non-oscillatory schemes of free surface flows. *Journal of Hydraulic Research* 1995; **33**(1):101–111.
17. Shu CW, Osher S. Efficient implementation of non-oscillatory shock-capturing schemes. *Journal of Computational Physics* 1988; **77**:439–471.
18. Zhou JG, Causon DM, Mingham CG, Ingram DM. The surface gradient method for the treatment of source terms in the shallow-water equations. *Journal of Computational Physics* 2001; **168**:1–25.
19. Harten A, Lax PD, van Leer B. On upstream differencing and Godunov-type schemes for hyperbolic conservation laws. *SIAM Review* 1983; **25**:35.
20. van Leer B, Lee WT, Powell KG. Sonic point capturing. *9th CFD Conference*, American Institute of Aeronautics and Astronautics, Buffalo, NY.
21. Bradford SF, Sandres BF. Finite-volume model for shallow-water flooding of arbitrary topography. *Journal of Hydraulic Engineering* (ASCE) 2002; **128**:289–298.
22. Toro EF. Shock *Capturing Methods for Free Surface Shallow Flows*. Wiley: New york, 2000.
23. Goutal N, Maurel F (eds). *Proceedings of the 2nd Workshop on Dam-Break Wave Simulation*, HE-43/97/016/B, France, 1997.
24. Hu K, Mingham CG, Causon DM. Numerical simulation of wave overtopping of coastal structures using the non-linear shallow water equations. *Coastal Engineering* 2000; **41**:433–465.
25. Hubbard ME, Garcia-Navarro P. Flux difference splitting and the balancing of source terms and flux gradients. *Journal of Computational Physics* 2000; **165**:89–125.
26. Brufau P, Vazquez-Cendon ME, Garcia-Navarro P. Numerical model for the flooding and drying of irregular domains. *International Journal for Numerical Methods in Fluids* 2002; **39**:247–275.
27. Batina J. Implicit flux-split euler schemes for unsteady aerodynamics analysis involving unstructured dynamic meshes. *AIAA* 1990; **29**(11):1361–1369.

